Electronic Supplementary Information for:

Direct nitrogen fixation at the edges of graphene nanoplatelets as efficient electrocatalysts for energy conversion

In-Yup Jeon,[1,†] Hyun-Jung Choi,[1,†] Myung Jong Ju,[2,†] In Taek Choi,[2] Kimin Lim,[2] Jaejung Ko,[2] Hwan Kyu Kim,[2] Jae Cheon Kim,[3] Jae-Joon Lee,[3] Dongbin Shin,[1] Sun-Min Jung,[1] Jeong-Min Seo,[1] Min-Jung Kim,[1] Noejung Park,*[,1] Liming Dai*[,1,4] and Jong-Beom Baek*[,1]

[1] Ulsan National Institute of Science and Technology (UNIST), Interdisciplinary School of Green Energy/Low-Dimensional Carbon Materials Center, Ulsan 689-897, South Korea

[2] Department of Advanced Materials Chemistry, Korea University, Sejong 339-700, South Korea

[3] Department of Applied Chemistry, Konkuk University, Chungju 380-701, South Korea

[4] Department of Macromolecular Science and Engineering, Case Western Reserve University, 10900 Euclid Avenue, Cleveland, Ohio 44106, USA.

* To whom correspondence should be addressed. E-mail: jbbaek@unist.ac.kr (J.-B. Baek), noejung@unist.ac.kr (N. Park), liming.dai@case.edu (L. Dai)

[†] Authors contributed equally.

Experimental

Instrumentations. Fourier transform infrared (FTIR) spectra were recorded on Perkin-Elmer Spectrum 100 using KBr disks. Themogravimetric analysis (TGA) was conducted on a TA Q200 (TA Instrument) under nitrogen at a heating rate of 10 °C/min. The surface area was measured by nitrogen adsorption/desorption isotherms using the Brunauer-Emmett-Teller (BET) method on Micromeritics ASAP 2504N Surface Area and Porosity Analyzer. The field emission scanning electron microscopy (FE-SEM) was performed on FEI Nanonova 230 while the high-resolution transmission electron microscopy (HR-TEM) employed in this work is a JEOL JEM-2100F (Cs) microscope operating at 200 kV. The TEM specimen were prepared by dipping carbon micro-grids (Ted Pella Inc., 200 Mesh Copper Grid) into well-dispersed samples in ethanol. X-ray photoelectron spectra (XPS) were recorded on a Thermo Fisher K-alpha XPS spectrometer. Elemental analysis (EA) was conducted with Thermo Scientific Flash 2000. Zeta-potential values were determined using a Malvern Zetasizer (Nano ZS, Malvern Instruments). X-Ray diffraction (XRD) patterns were recorded with a Rigaku D/MAZX 2500V/PC with Cu–Kα radiation (35 kV, 20 mA, λ = 1.5418 Å). Raman spectra were taken with a He-Ne laser (532 nm) as the excitation source by using confocal Raman microscopy (Alpha 300S, WITec, Germany), in conjunction with atomic force microscopy (AFM).

DFT Calculations. For computations, we used the Vienna Ab initio Simulation Package(VASP) to calculate the ground state ofmany electrons system in the frame work of density functional theory[S1-S4]. The plane-wave basis set with anenergy cut-off of 400 eV and the PBE-type gradient-corrected exchange-correlation potential were employed[S5].

Photochemical Study on DSSCs. Homogenously dispersed 0.1 wt% NGnPs in 2-propanol solution was obtained by ultrasonication for 30 min. The resulting solution was deposited directly onto FTO/glass (TEC-8, Pilkington) using an e-spray technique. First, the NGnPs solution was loaded in a plastic syringe equipped with a 30-gauge stainless steel hypodermic needle. The needle was connected to a high voltage power supply (ESN-HV30). A voltage of ~6.5 kV was applied between a metal orifice and the conducting substrate at a distance of 10 cm. The feed rate was controlled by the syringe pump at a constant flow rate of 150μL min^{-1}.As can be seen at SEM images presented in **Figs.S8b** and **S8c**, it is clearly discriminate that the FTO surface is covered with the NGnPs. For comparison, a conventional Pt CE was prepared by deposition of *ca.* 20μL/cm^2 of H_2PtCl_6 solution (2 mg of Pt in 1 mL of ethanol) and sintered at 400 ℃ for 15 min.

To investigate the cathodic performance at conditions which are as close as possible to the actual situation in DSSC, the symmetrical sandwich dummy cellswere fabricated from two identical NG-FTO or Pt-FTO sheets, which were separated by 60 μm thick Surlyn (Solaronix, Switzerland) tape as a seal and spacer leaving 0.6 × 0.5 cm^2 active area. The cell was filled with an electrolyte solution through a hole in one FTO support which was finally closed by a Surlyn seal. The FTO sheet edges were coated by ultrasonic soldering (USS-9200, MBR Electronics) to improve electrical contacts.

FTO plates were cleaned in detergent solution, water, and ethanol using an ultrasonic bath. The FTO substrates were immersed in 40 mM aqueous $TiCl_4$ solution at 70 ℃ for 30 min and washed with water and ethanol. A TiO_2 colloidal paste (Dyesol, 18NR-T) was screen-printed onto FTO/glass and sintered at 500 ℃ for 30 min in air. The thickness of the transparent layer was measured byusing an Alpha-step 250 surface profilometer (Tencor Instruments, San Jose, CA), and a paste for the scattering layercontaining 500 nm sized anatase particles (ENB Korea, STP-500N) was deposited by doctor blade printing and

thendried at 25℃ for 2 h. The TiO_2 electrodes were sintered at 500℃ for 30 min. The resulting TiO_2 photoanode was immersed in a THF/ethanol (v/v, 1/2) solution containing 0.3 mM of *O*-alkylated-JK-225 dye[S6]and 0.3 mM of multi-functional coadsorbent HC-Aand kept at room temperature for 12 h. The dye adsorbed TiO_2 photoanodes were assembled with NG or Pt CEs using a thermal adhesive film (60 μm thick Surlyn, Du-Pont) as a spacer to produce a sandwich-type cell. The electrolyte solution was 0.22 M $Co(bpy)_3(BCN_4)_2$, 0.05 M $Co(bpy)_3(BCN_4)_3$, 0.1 M $LiClO_4$, and 0.8 M 4-*tert*-butylpyridine in acetonitrile. Co-complexes were synthesized with the literature procedure[S7].Electrolyte solution was introduced through a drilled hole on the CE*via* vacuum backfilling. The hole was sealed with cover glass usingSurlyn.

Photoelectrochemical data were measured using a 1000 W xenon light source (Oriel, 91193) that was focused togive 100 mW cm^{-2},which is the equivalent of one sun at Air Mass (AM) 1.5Gat the surface of the test cell. The lightintensity was adjusted with a Si solar cell that was doubled-checked with an NREL calibrated Si solar cell (PVMeasurement Inc.). The applied potential and cell current were measured using a Keithley model 2400digital source meter. The current-voltage characteristics of the cell under these conditions weredetermined bybiasing the cell externally and measuring the generated photocurrent. This process was fully automated usingWavemetrics software.The measurement-settling time between applying a voltage and measuring a current for the *J*–*V* characterization of DSSCs was fixed to 40 ms.

Evaluation of Electrocatalytic Activities with EIS and CA. The electrocatalytic activity of the CE in DSSCs can be conveniently evaluated by using a symmetrical dummy cell (**Fig. S9b**) through EIS technique, in which a thin layer of the electrolyte solution is sandwiched between two identical electrodes to be tested as CEs of the DSSCs. In general, the

impedanceof a dummy cell can be fitted to the equivalent circuit shown in **Fig. 4a**, whereR_S is the ohmic serial resistance, R_{CT} is the charge transfer resistance at the CE/electrolyte interface, CPE is a constant phase element describing deviation from the ideal capacitance due to the roughness of the electrode surface[S8-S11], and Z_W is the Nernst diffusion impedance in the bulk electrolyte solution. The $R_{CT}$is a useful parameter to evaluate the catalytic performance of the CE materials in DSSCs.It is due to the fact that the exchange current density, J_0 (*i.e.*, the equal cathodic and anodic currents normalized to the projected electrode area at equilibrium), should be akin to the photocurrent density on the TiO_2 photoanode working under full sun illumination on a CE. J_0 varies inversely with R_{CT},which can be described in eq. (1)[S12], in which *R*is the gas constant, *T*is the absolute temperature, *n* is the number of electrons, and *F* is the Faraday constant.If the CE has a J_0 of 20 mA/cm^2, this J_0 valuecorresponds to an R_{CT} = 1.3 Ω cm^2 (n = 1) at room temperature as described in eq. (1)[S12].

$$J_0 = \frac{RT}{nFR_{CT}} \qquad (1)$$

For the Pt and NGnP CEs, the R_{CT} values calculated were 1.9 and 2.6Ω cm^2, respectively.The corresponding J_0 values, calculated from eq. (1), were 10.3 and 9.88 mA/cm^2, respectively. The results are in good agreement with the reported values for $Co^{3+/2+}$ mediated electrolytes[S13,S14], demonstrating that the electrochemical $Co(bpy)_3^{3+}$ reduction on the NGnP-FTO CE was significantly enhanced compared with that of the Pt-FTO CE.Moreover, the lower serial resistance (R_S) of NGnP-FTO electrode compared to that of Pt-FTO electrode was obviously due to the conductive FTO support as described in eq. (2).

The impedance of a CPE (Z_{CPE}) is:

$$Z_{CPE} = B(j\omega)^{-\beta} \qquad (2)$$

where B and β are frequency independent parameters of CPE ($0 \leq \beta \leq 1$; for $\beta = 1$, the Z_{CPE} transforms into capacitance at the electrical double-layer).For the NGnP-FTO electrode,

fitting of the first high frequency region semicircle provided the following values: R_S = 1.1 Ω cm^2, R_{CT} = 1.9 Ω cm^2, $1/B = 1.9 \times 10^{-4}$ $S.s^{\beta}$, and β is 0.77. For the Pt-FTO electrode, these values are summarized in **Table S5**.

The Nernst impedance Z_W to mass transfer is given by the Warburg impedance in the electrolyte solution as described in eq. (3):

$$Z_W = \frac{W}{\sqrt{j\omega}} tanh\sqrt{\frac{j\omega}{K_N}} \qquad (3)$$

where W is the Warburg parameter and K_N is $D/0.25\delta^2$[S8]. At zero bias, the curve fitting of the second semicircles from the Nyquist plots to Z_W with an equivalent circuit allows the determination of the $Co(bpy)_3^{3+/2+}$ diffusion coefficients, which were found to be 4.5×10^{-6} cm^2/s for the NGnP-FTO dummy cell and 3.2×10^{-6} cm^2/s for the reference Pt-FTO. The similar $Z_W$impedance values between the NGnP-FTO and Pt-FTO electrodes for mass transfer indicated that ionic diffusion in the bulk electrolyte solution is independent of the catalytic activity of the electrodes.

Another technique for characterization of mass transport in the electrolyte solution is potential-step chronoamperometry (CA)[S8]. Extrapolation of bothlinear components of the CA plots providesintersection at the so-called transition time, τ which providesthe diffusion coefficient, D according to the eq. (4)[S8,S15].

$$D = \frac{\delta^2}{4\pi\tau} \qquad (4)$$

From the data in **Fig.9a** and eq.(4), we can calculate diffusion coefficient of $Co(bpy)_3^{3+}$. Similar diffusion coefficient values for mass transfer between NGnP-FTO and Pt-FTO electrodes indicated that ionic diffusion in the bulk electrolyte solution is independent of the catalytic activity of the electrodes.

Electrochemical Measurements. The electrochemical tests were carried out using a computer-controlled potentiostat (1470E Cell Test System, Solartron Analytical, UK) with a typical three-electrode cell. A platinum wire was used as a counter-electrode and an Ag/AgCl (3 M KCl filled) electrode as the reference electrode. All the experiments were conducted at ambient condition. The working electrodes were prepared by applying respective catalyst inks onto the prepolished glassy carbon (GC) disk electrodes. Briefly, samples were dispersed in ethanol and ultrasonicated for 15 min to form uniform catalyst inks (2 mg mL^{-1}). A total of 7.5 µL of a well-dispersed catalyst ink was applied onto a pre-polished glassy carbon (GC) disk electrode (5 mm in diameter). After drying at room temperature, Nafion (0.05 wt%) stock solution (5 µL) in ethanol was applied onto the surface of the catalyst layer to form a thin protective film[S16]. The addition of a small amount of Nafion could effectively improve the dispersion of catalyst suspension. The electrodes thus prepared were dried at room temperature overnight prior tothe electrochemical tests.

The detailed kinetic analysis was conducted according to Koutecky-Levich plots in eq. (5):

$$\frac{1}{j} = \frac{1}{j_k} + \frac{1}{B\omega^{0.5}} \quad (5)$$

where j_k is the kinetic current and B is Levich slope which is given by eq. (6):

$$B = 0.2nF(D_{O_2})^{2/3}v^{-1/6}C_{O_2} \quad (6)$$

Here n is the number of electrons transferred in the reduction of one O_2 molecule, F is the Faraday constant (F = 96485 C/mol), D_{O2} is the diffusion coefficient of O_2 (D_{O2} =1.9×10^{-5} cm^2 s^{-1}), ν is the kinematics viscosity for KOH (v = 0.01 cm^2 s^{-1}) and C_{O2} is concentration of O_2 in the solution (C_{O2} = 1.2 × 10^{-6} mol cm^{-3}). The constant 0.2 is adopted when the rotation speed is expressed in rpm. According to equations (5) and (6), the number of electrons transferred (n)[S17]can be obtained from the slope of Koutecky-Levich plot of i^{-1}*vs.*$\omega^{-1/2}$. From

published data[S18,S19] for F (96485 C mol^{-1}), D_{O2} (1.9×10^{-5} cm^2 s^{-1}), υ(0.01 cm^2 s^{-1}), and C_{O2} (1.2×10^{-6} mol cm^{-3}), B is calculated to be 0.144 mA $s^{-1/2}$ at A=0.19625 cm^2 for a four-electron exchange reaction (n = 4).

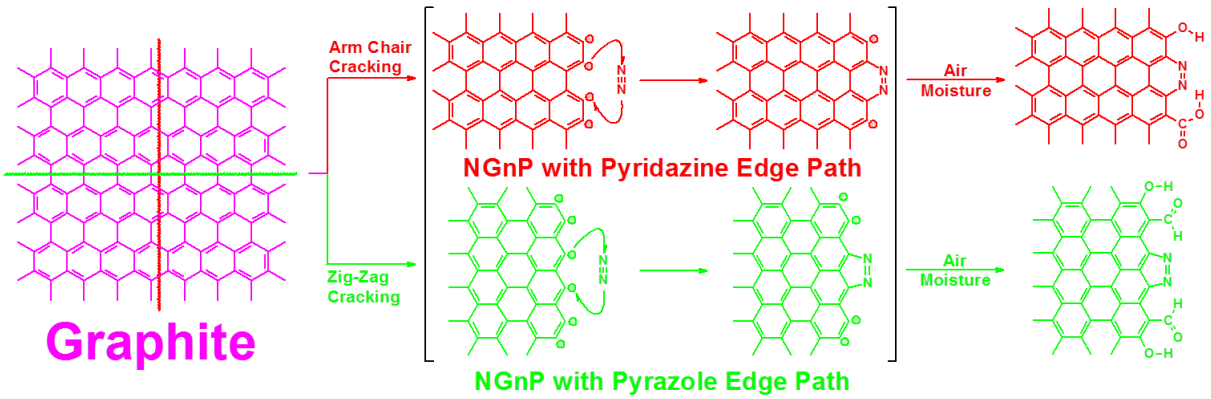

Figure S1. Proposed mechanism for the reaction between graphite and nitrogen in a ball mill crusher and subsequent termination of remnant activated carbons in air moisture upon opening the crusher. Depending upon cracking patterns, such as zigzag and armchair, the edges are expected to form pyrazole and pyridazine rings, respectively, from the cyclization between activated edges and nitrogen.

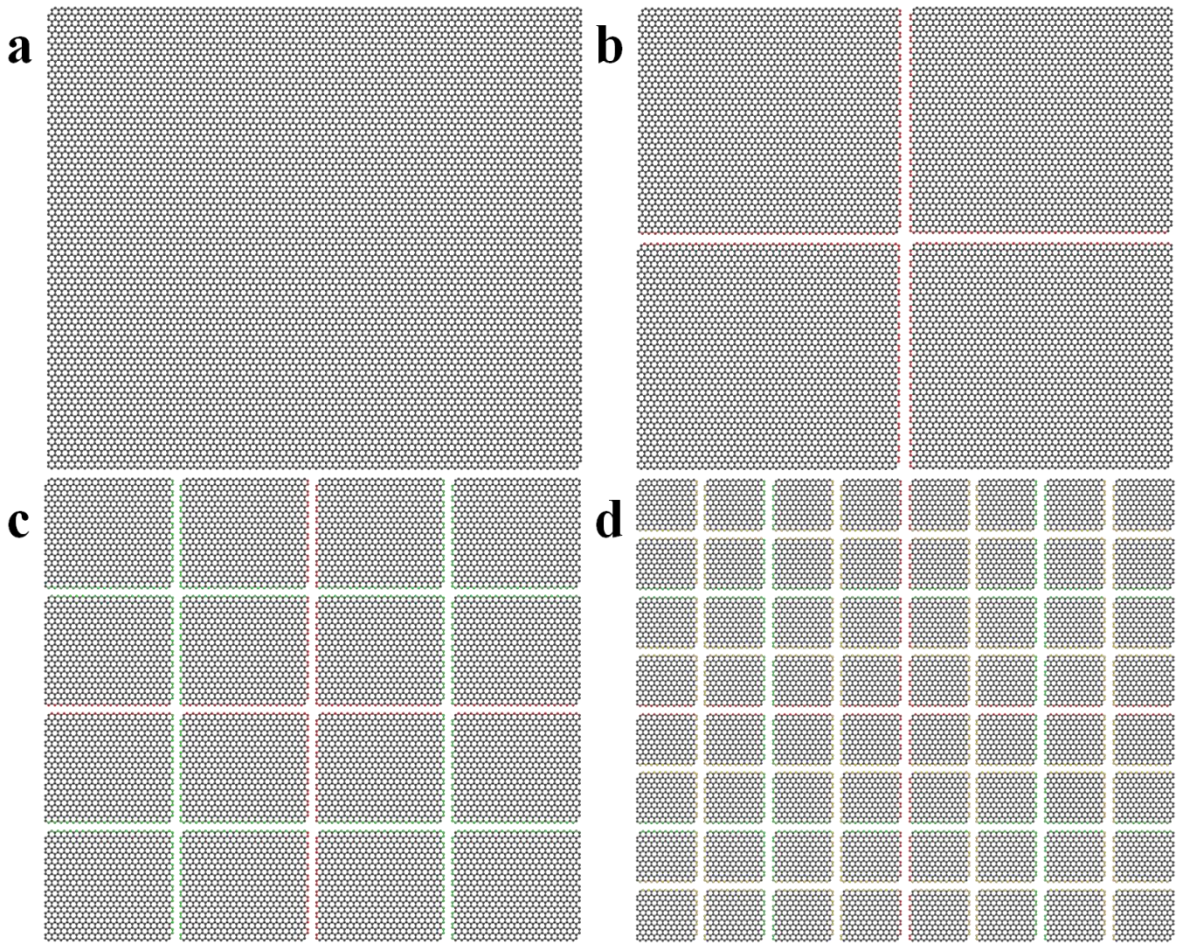

FigureS2. Proposed universal cracking model for the ball-milling-induced edge-functionalization of graphite: (a) a graphene plateletwith 100 carbon atoms at an edge; (b) the first crosscutting (red) into 4 pieces, generating 400 active carbon atoms; (c) the second crosscutting (green) into 16 pieces. Total 1200 active carbon atoms are generated; (d) the third crosscutting (yellow) into 64 pieces with 2800 active carbon atoms. The graphitic structure is simplified for the reason of clarity.

The amount of fixed nitrogen *versus*the grain size reduction could be correlated by establishing a cracking model. As the starting graphite (~150 μm, **Fig. 1b**) is much larger than the ball-milled NGnPs (<1 μm, **Fig. 1c**), the ratio of edge/basal carbon atoms dramatically increases as the grain size reduces. For example, the total carbon numbers

are10,000 for a square-shaped graphene with 100 carbons at each edge (**Fig. 2a**). Upon crosscutting it into 4 squares (**Fig. S2b**), the available additional active carbon atoms at the edges are 400 (Out of total 800 carbon atoms at the edges.) as each cut generates 200 active carbon atoms at the edges. Now, the percent of active carbon atoms at the edges out of total carbonatoms becomes 4%(400/10000 × 100%).The second crosscutting of the 4 pieces into 16 pieces (**Fig. S2c**) leads to the available active carbon atomsare 1200, and hence the percent of active carbon atoms is 12%. Subsequent crosscutting leads to 64 pieces with 28% active carbons (**Fig. S2d**). Total active carbon atoms could be calculated by following eq. (5):

$$8a\sum_{k=1}^{n}\left(\frac{1}{2}\right)^{k}\cdot 4^{k-1} = 2a\sum_{k=1}^{n}2^{k} \qquad (5)$$

where the *k* is the number of crosscutting and the *a* is the initial average number of carbon atoms at the edges. As can be seen, the available number of active carbon atoms at the broken edges exponentially increases as an average grain size reduces. This leads to a high nitrogen content at the edges, though not all active carbon atoms could react with nitrogen.

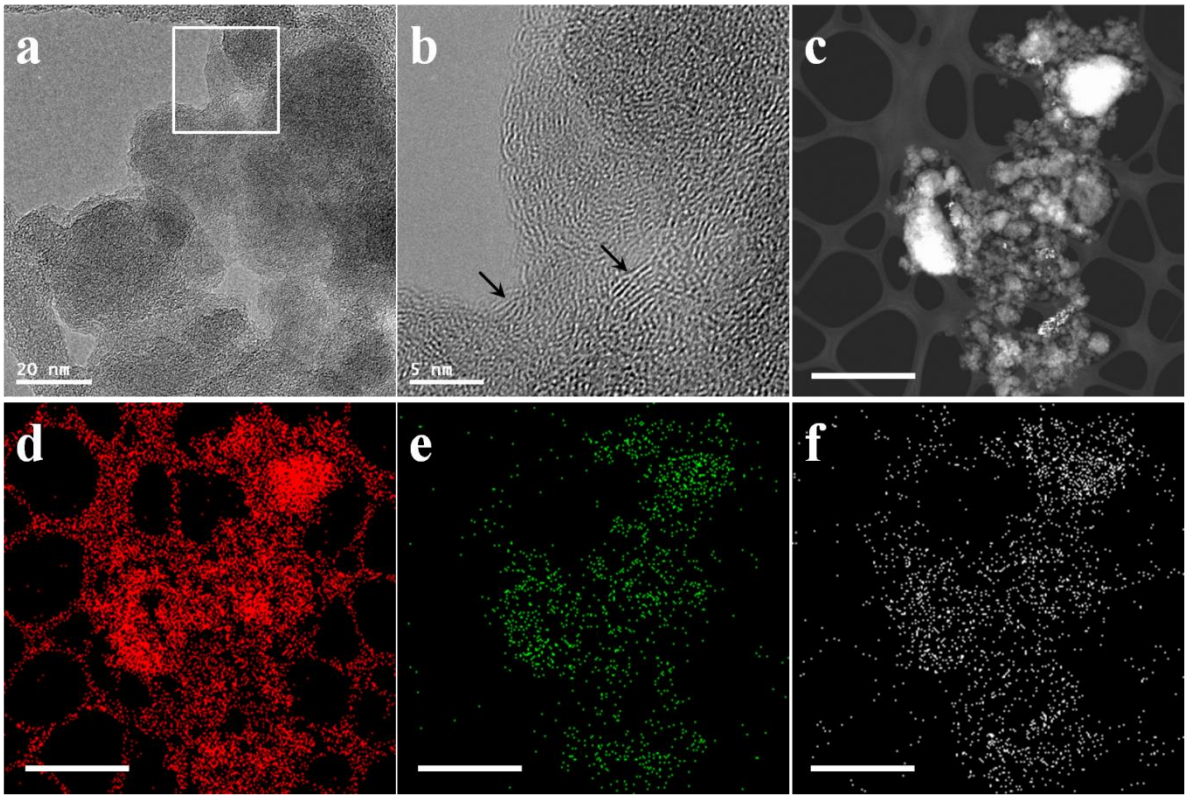

Figure S3. (a) TEM image of NGnPs; (b) the edge-on view of square in (A) at higher magnification, showing stripes (arrows) indicating high crystallinity; (c) dark field TEM image. Corresponding element mappings from (c): (d) carbon; (e) nitrogen; (f) oxygen. Scale bars are 1 μm.

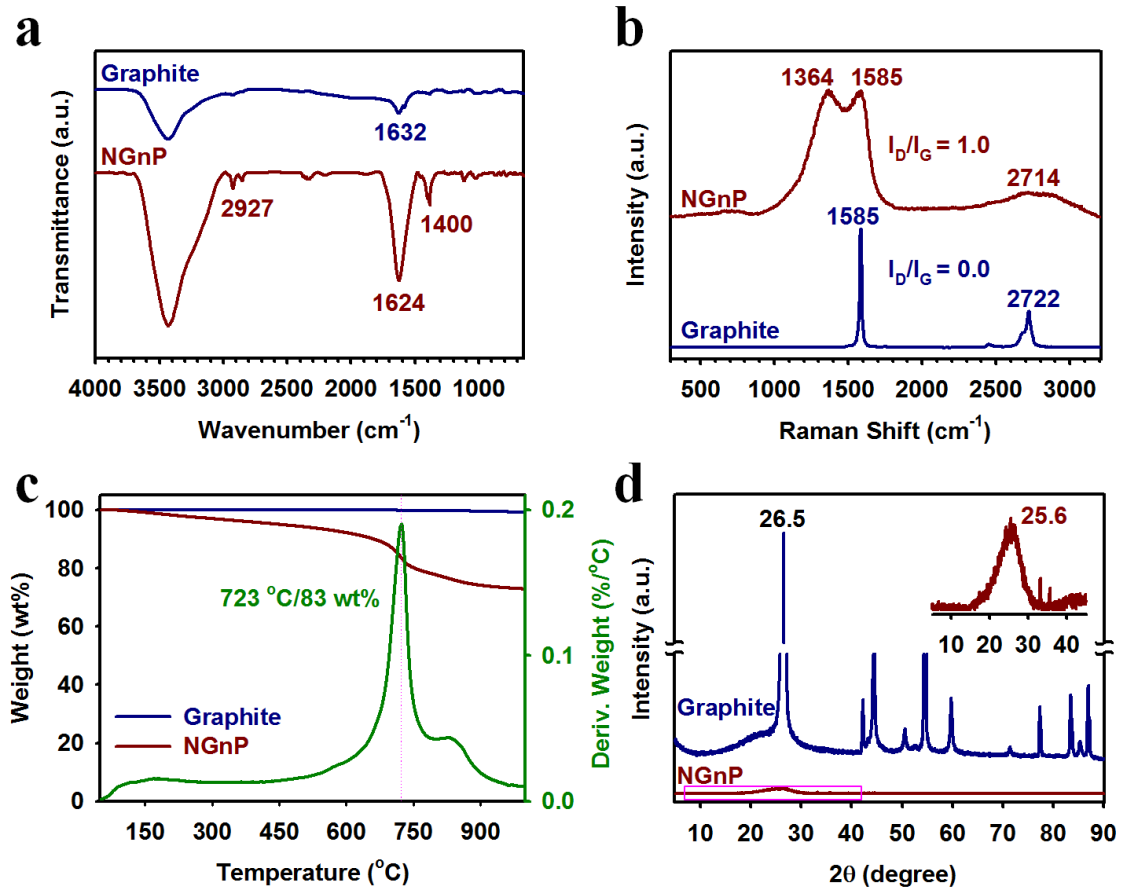

Figure S4.(a) FT-IR spectra (KBr pellets), showing clear C=N stretching peak at 1400 cm^{-1}; (b) Raman spectra obtained from a He-Ne laser (532 nm) as the excitation source;(c) TGA thermograms obtained at the heating rate of 10 ℃/min in argon; (d) XRD diffraction patterns. Inset is magnified pattern of pink rectangle.

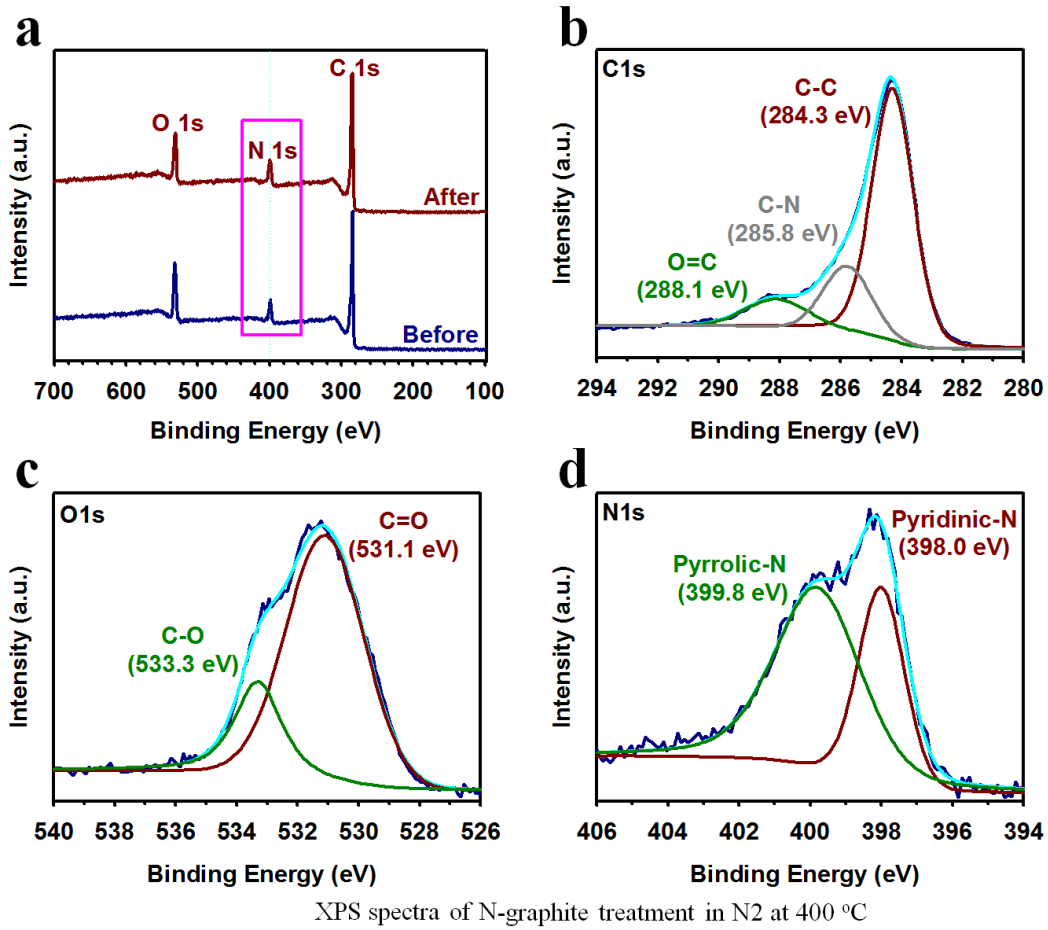

Figure S5. XPS survey of NGnPs: (a) full spectra of before andafter heat-treatment at 400 ℃ under argon atmosphere for 2h. High-resolution XPS spectra: (b) C1s; (c) O1s; (d) N 1s.

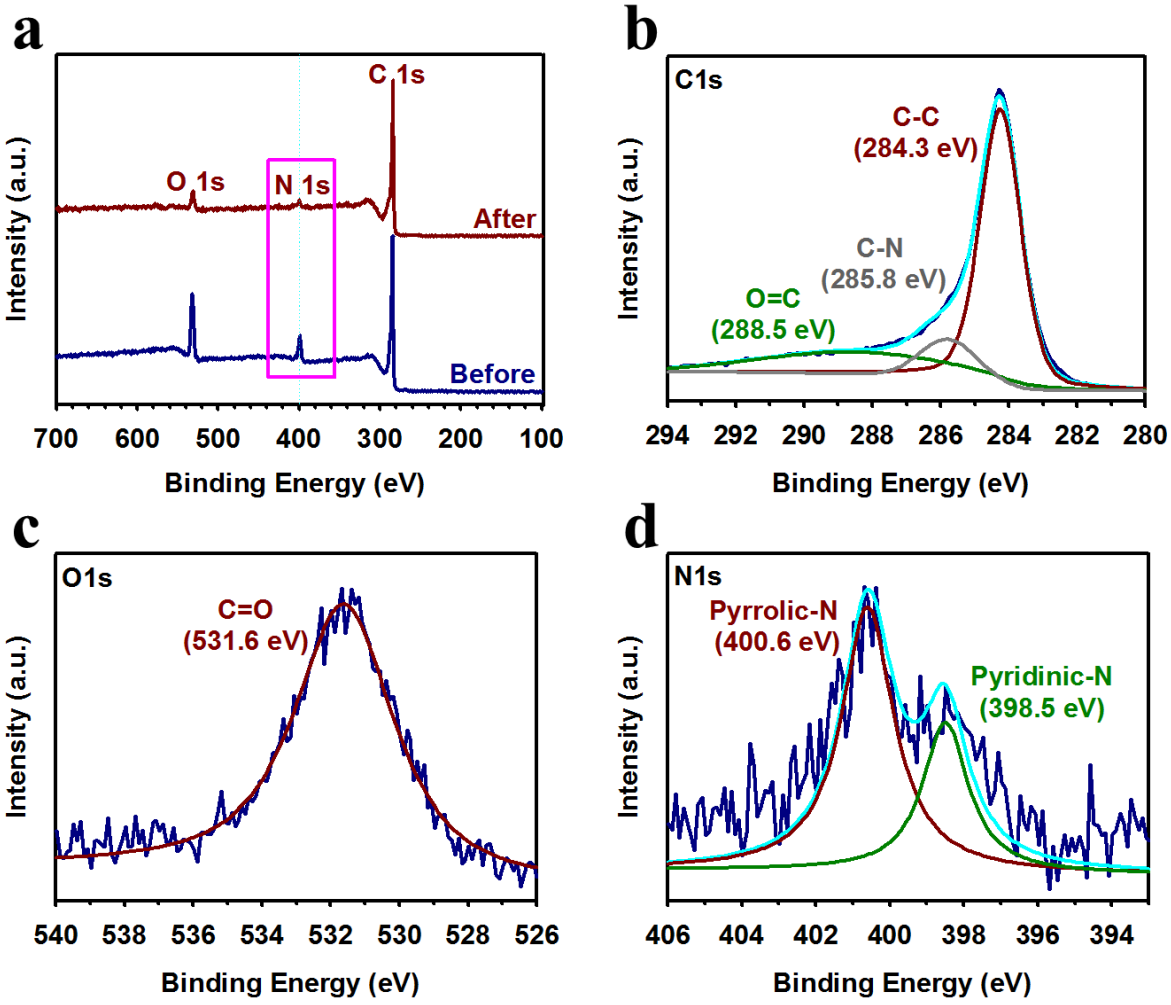

Figure S6. XPS survey of NGnPs: (a) full spectra of before andafter heat-treatment at 1000 ℃ under argon atmosphere for 2h. High-resolution XPS spectra: (b) C1s; (c) O1s; (d) N 1s.

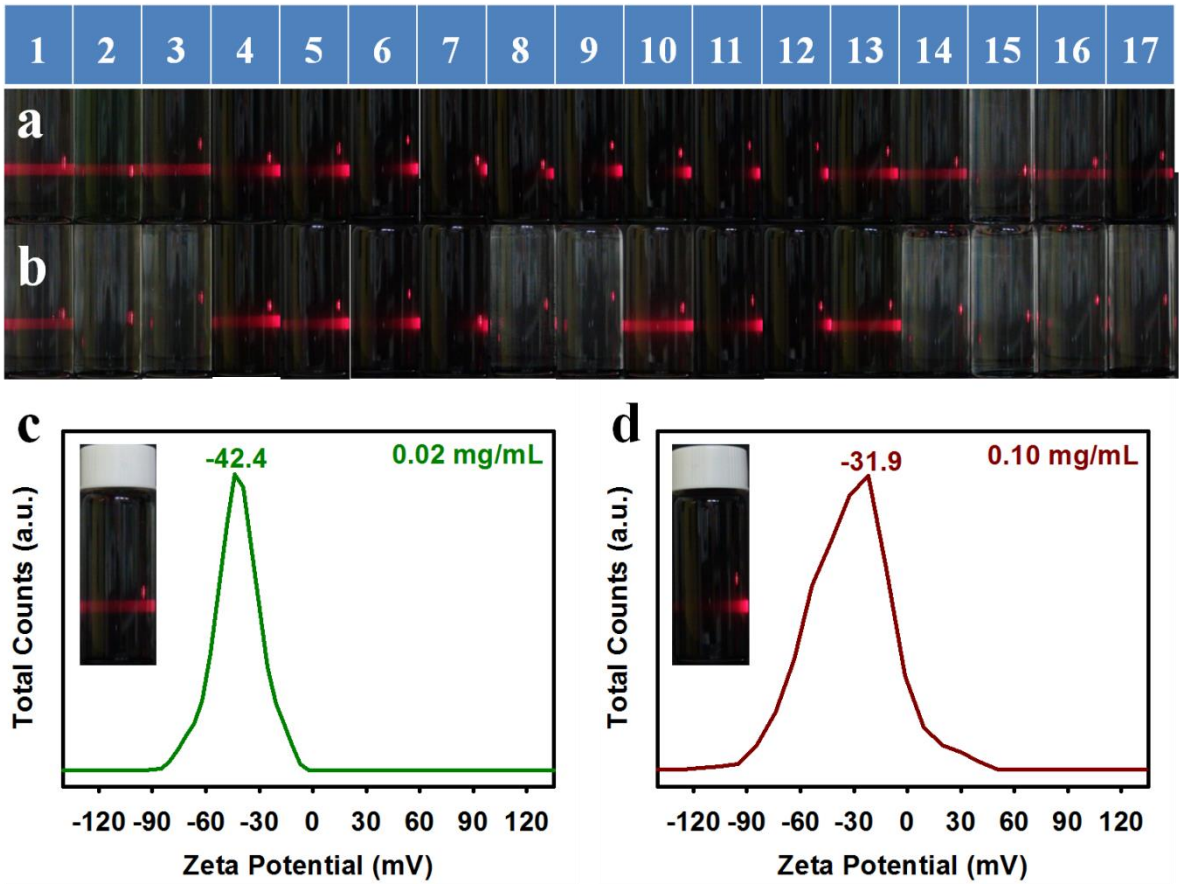

Figure S7. Photographs of NGnPs dispersed solutions in various solvents in a normal laboratory condition: (a) after 30 seconds; (b) after one week standing on bench top: (1) H_2O; (2) 1M HCl; (3) 1M KOH; (4) 1M NH_4OH; (5) 7M NH_4OH; (6) MeOH; (7)isopropanol; (8)ethylacetate; (9) THF; (10) Acetone; (11) DMAc; (12) DMF; (13) NMP; (14) CH_2Cl_2; (15) Toluene; (16) Hexane; (17) CS_2. Zeta-potentials of NGnPs in DMAc at different concentrations: (c) 0.02 mg/mL; (d) 0.10 mg/mL. Insets are the photographs of NGnPs at given concentrations.

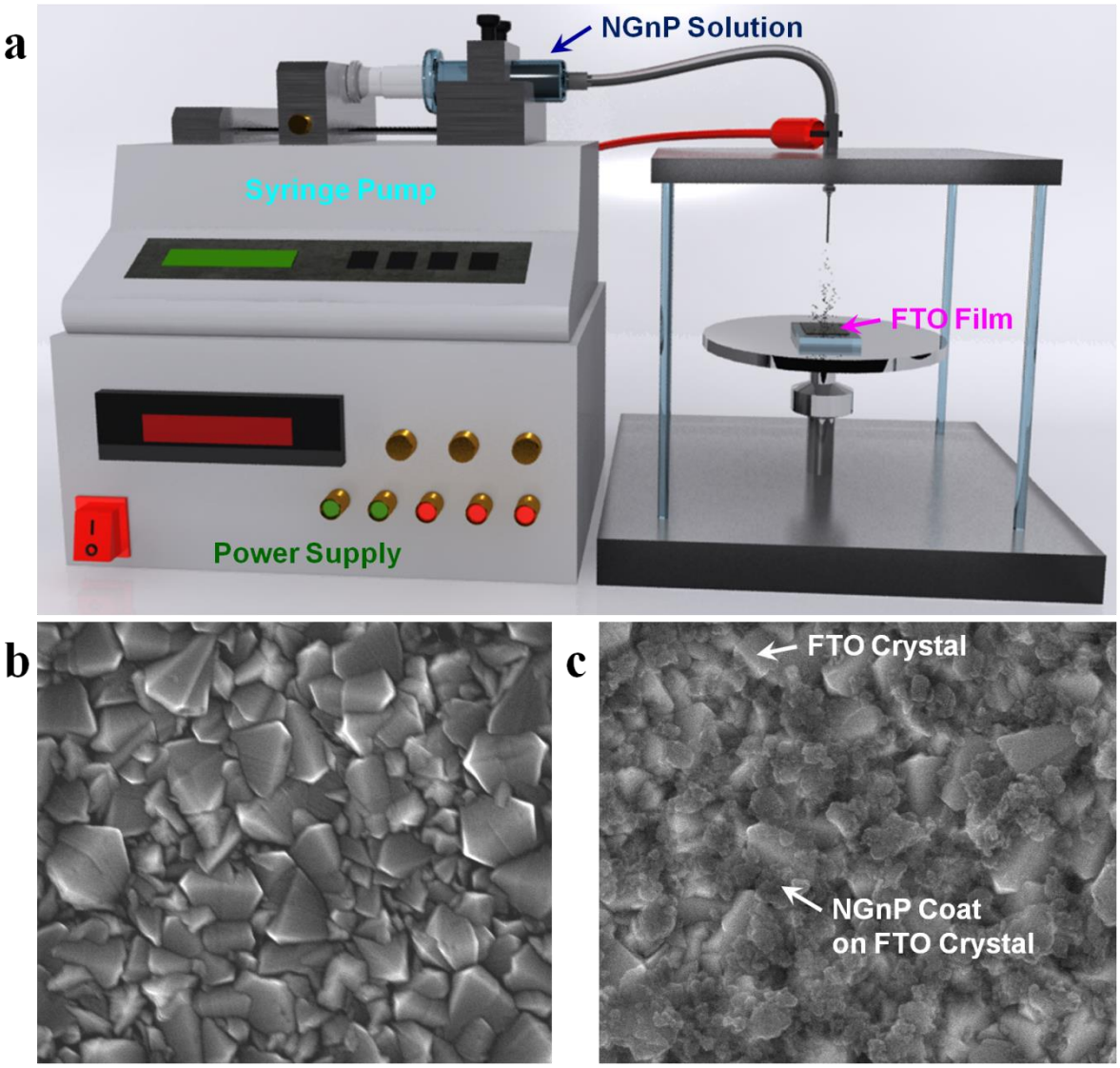

FigureS8.(a) Schematic presentation of the e-spray setup for NGnP deposition on the FTO/glass substrates. SEM images: (b) bare FTO; (c) NGnP-FTO. Scale bars are 1 µm.

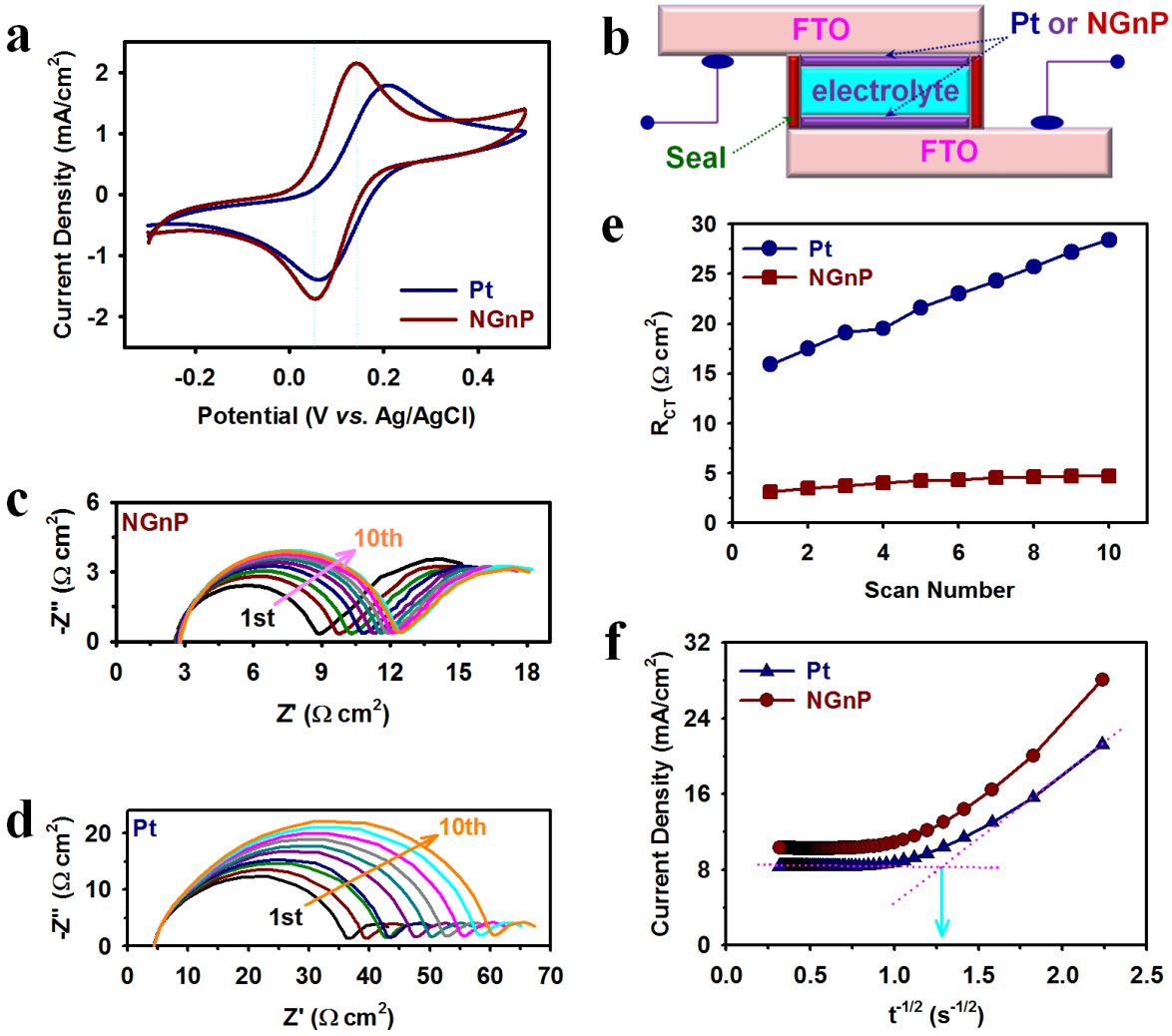

Figure S9.(a) Cyclic voltammograms (CV) obtained at a scan rate of 0.01 V/s for the oxidation and reduction of the $Co(bpy)_3^{3+/2+}$ redox couple using the Pt-FTO and NGnP-FTO as the working electrodes, a Pt wire as the CE, Ag/Ag^+ as the reference electrode, and 0.1 M $LiClO_4$ was used as supporting electrolyte. (b) Typical structure of a symmetrical dummy cell using two identical electrodes for ESI stability and CA measurements. Electrochemical stability under cycling potential on symmetrical dummy cells with $Co(bpy)_3^{3+/2+}$ solution in acetonitrile: (c) NGnP-FTO; (d) Pt-FTO. The sequence of measurements was as follows: 5 × CV scans (from 0 V → 1 V → −1 V → 0 V→1V, scan rate 0.05 V/s) followed by 30 s relaxation at 0 V and by EIS measurement at 0 V from 10^6 Hz to 0.1 Hz. This sequence of electrochemical stability test was repeated 10 times. (e) Plots of R_{CT} verses scan number,

showing R_{CT} values of Pt-FTO linearly increase with respect to scan number, while those of NGnP-FTO remain almost constant. (f) CA plots on symmetrical dummy cells with two Pt-FTO and NGnP-FTO electrodes in $Co(bpy)_3^{3+/2+}$ solution in acetonitrile at an applied bias potential of 0.75 V for 10 s.

To examine the electrochemical stability of electrodes, freshly assembled dummy cells were first measured with electrochemical impedance spectra (EIS) at room temperature, and then the dummy cells were subjected to CV cycles followed by EIS measurements. The electrochemical stability of NGnP dummy cell under cycling potential shows that there were no noticeable changes in either R_S in the high frequency region or the semicircles in the low frequency region (**Figs. S9c** and **S9e**), while R_{CT} of Pt is linearly increasing with respect to scan number (**Figs. S9d** and **S9e**). These results indicate there is no influence of cycling potential on the R_S or the mass transport in the electrolyte solution for the NGnP electrode.

To further examine mass transfer properties in the same electrolyte solution, chronoamperometry (CA) measurements were carried out at room temperature. Shortly after the potential step, the current follows the semi-infinite Cottrell-like decay(**Fig.S9f**)[S15]. Hence, the mass transfer *D* values for NGnP- and Pt-FTO electrodes were calculated to be1.58×10^{-6} and 1.64×10^{-6} cm^2s^{-1}, respectively, indicating that ionic diffusion in the bulk electrolyte solution is also independent of the catalytic activity of the electrodes.

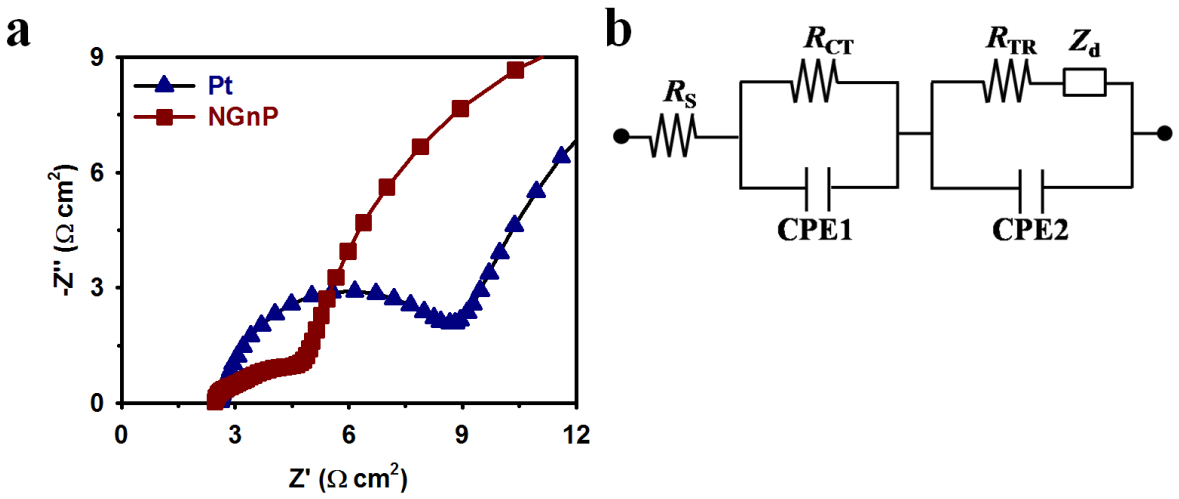

FigureS10. (a) Nyquist plots of the DSSCs with NGnP- and Pt-FTO CEs at a forward bias of –0.85 V under dark condition from 10^6 Hz to 0.1 Hz. Solid lines are fitted lines. (b) Equivalent circuit for EIS data fitting.

In typical EIS analysis, R_S of DSSCs is generally composed of at least three internal resistances (**Fig. S10b**)[S15,S16,S20,S21]. The semicircles in the different frequency regions indicate the Nernst diffusion limited impedance of the redox species in the electrolyte, impedance by transport and recombination competition occurred at the TiO_2/dye/electrolyte interface (R_{TR}), and charge transfer resistance at the CE/electrolyte interface (R_{CT}). The semicircle at the highest frequency region in **Fig.S10a** is related to the CE/electrolyte event, and the R_{CT} at the CE/electrolyte interface can be obtained from the real component values. The R_{CT} values of the DSSC with Pt-FTO and NGnP-FTO CEs are summarized in **Table S7**. For the NGnP-FTO CE, the lower R_{CT} value exhibited compared to that of Pt-FTO CE, and it might allow of an increase in fill factor of DSSC.

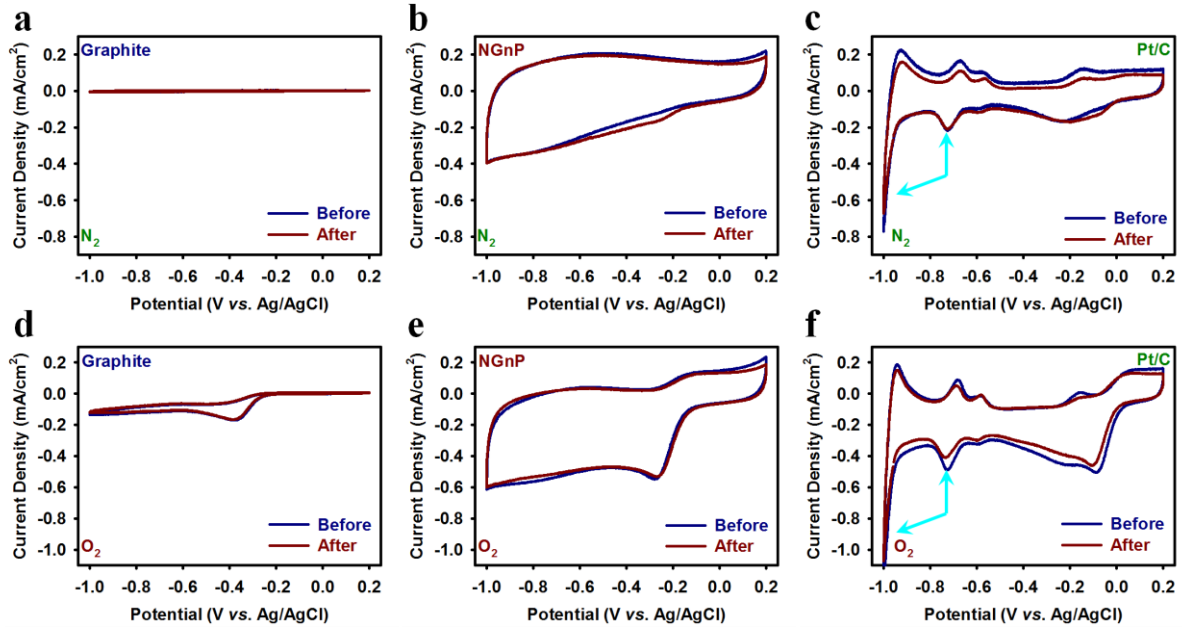

Figure S11. Cyclic voltammograms (CVs) of samples on glassy carbon (GC) electrodes before and after 100 cycles with scan rate of 0.01 V/s in N_2-saturated 0.1 M aq. KOH solution: (a) graphite; (b) NGnPs; (c) Pt/C. Sky blue arrows indicate the contributions of hydrogen evolution at around-0.7 V and out of Pt limiting potential (-0.8 V). CVs of samples on glassy carbon (GC) electrodes before and after 100 cycles with scan rate of 0.01 V/s in O_2-saturated 0.1 M aq. KOH solution: (d) graphite; (e) NGnPs; (f) Pt/C. Sky blue arrows indicate the contributions of hydrogen evolution at around-0.7 V and out of Pt limiting potential (-0.8 V).

To evaluate electrochemical stabilities of sample electrodes, we performed continuous chronoamperometric measurements at 0.01 V/s in both N_2- and O_2-saturated 0.1 M KOH solutions (**Figs. S11-S13** and **Table S8**)to test the cycle stability of the NGnP electrocatalyst. As can be seen in **Fig. S13**, the NGnP electrode exhibited a relatively slower decay in both N_2- and O_2-saturated electrolytes to retain 99.6 and 95.5% of their initial capacitances, respectively, even after 100 cycles in respect to the commercial Pt/C electrode (82.0 and 81.6% in the N_2- and O_2-saturated electrolytes, respectively).

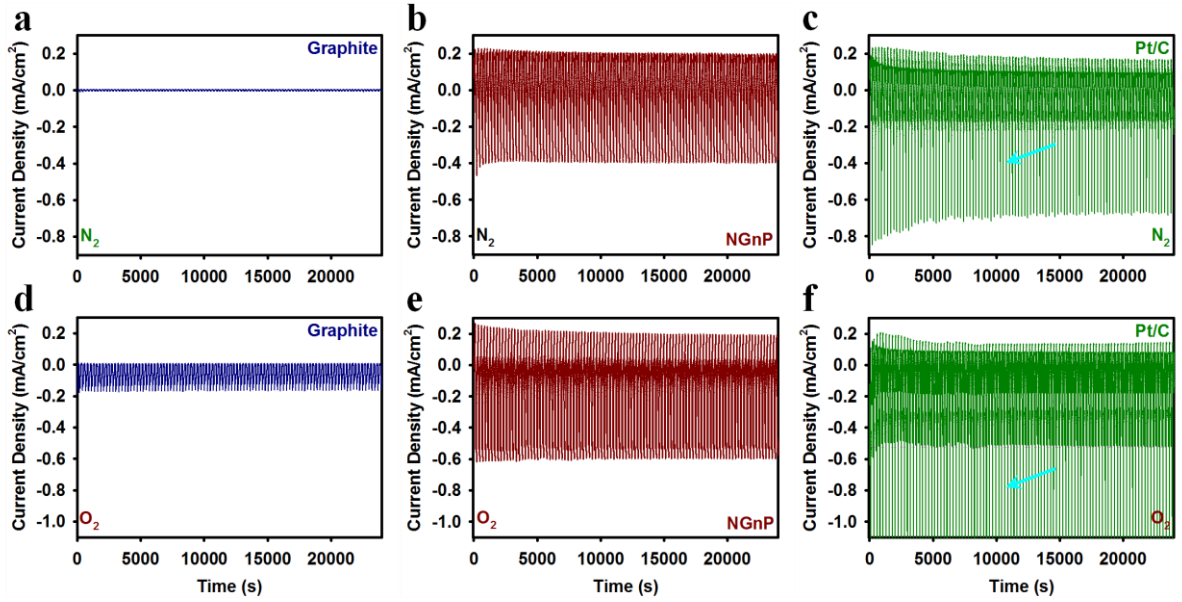

Figure 12. Current-time (*i*-*t*) chronoamperometric responses of sample electrodes at 0.01 V/s in N_2-saturated 0.1 M aq. KOH solution: (a)pristine graphite; (b) NGnPs; (c) Pt/C. Sky blue arrow indicates the contributions of hydrogen evolution at around -0.7 V and out of Pt limiting potential (-0.8 V). Current-time (*i*-*t*) chronoamperometric responses for the sample electrodes at 0.01 V/s in O_2-saturated 0.1 M aq. KOH solution: (d)pristine graphite; (e) NGnPs; (f) Pt/C. Sky blue arrow indicates the contributions of hydrogen evolution at around-0.7 V and out of Pt limiting potential (-0.8 V).

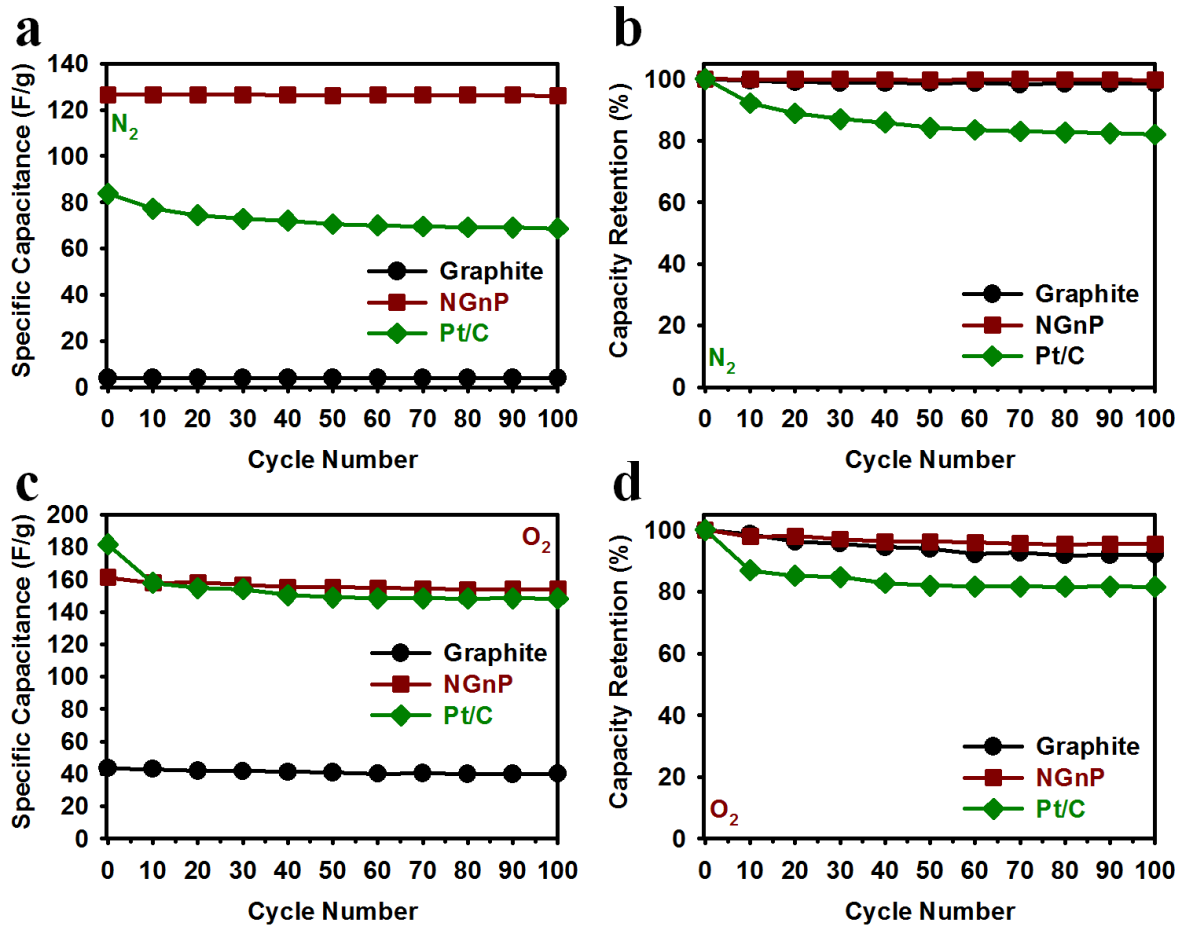

Figure S13. Cycle stability of sample electrodes with respect to cycle number in N_2-saturated 0.1 M aq. KOH solution with scan rate of 0.01 V/s: (a) capacitance changes *versus* the cycle number; (b) percent capacitance retention *versus* cycle number. Cyclic stability of samples with respect to cycle number in O_2-saturated 0.1 M aq. KOH solution with scan rate of 0.01 V/s: (c) capacitance changes *versus* the cycle number; (d) percent capacitance retention *versus* cycle number.

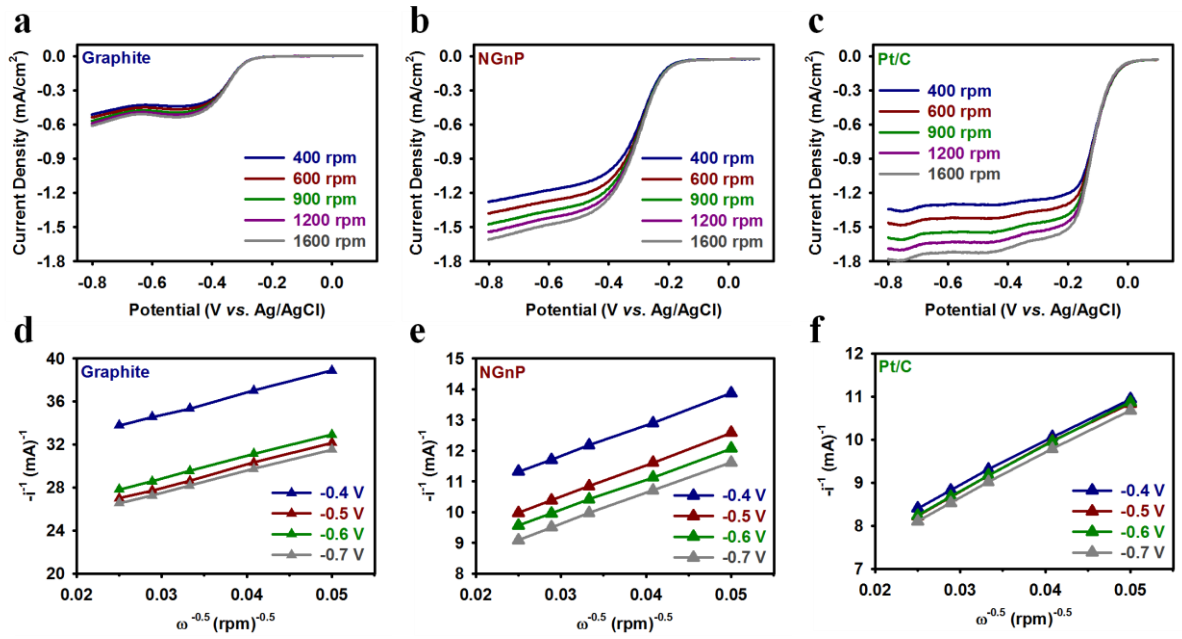

Figure S14.RDE voltammograms in O_2-saturated 0.1M aq. KOH solution with a scan rate of 0.1 V/s at different rotating rates: (a) pristine graphite; (b) NGnPs; (c) Pt/C. Koutecky-Levich plots derived from RDE measurements at different electrode potentials: (d) pristine graphite; (e) NGnPs; (f) Pt/C.

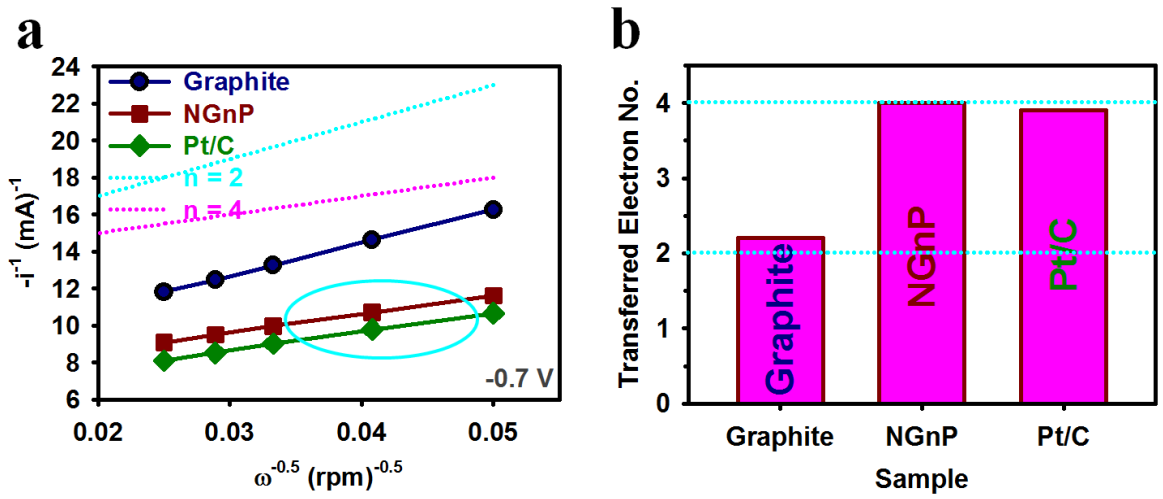

Figure S15.(a) Comparison of Koutecky-Levich plots derived from the RDE measurements at –0.7 V electrode potentials, showing NGnPs and Pt/C (sky blue oval) are very close to a four-electron transfer (n ~ 4) process (pink dotted line), while the pristine graphite is a classical two-electron transfer (n ~ 2) process (sky blue dotted line). (b) The numbers of electrons (n) transferred calculated from the limiting potential of Pt/C at –0.7 V.

Table S1. BET surface areas of the pristine graphite and NGnPs

Sample	Surface Area (m^2/g)	Pore Volume (mL/g)	Pore Size (Å)
Graphite	2.78	0.0016	22.7
NGnP	108.99	0.0529	19.4

Table S2. EA data of the pristine graphite and NGnPs

Sample	C (%)	H (%)	O (%)	N (%)	C/O	C/N
Graphite	99.64	BDL[a]	0.13	BDL	1021	NA
NGnP	70.67	0.79	7.43	14.84	11.3	5.6

a. BDL = Below detection limit.

b. NA = Not available

Table S3. XPS and TGA data of the pristine graphite and NGnPs

Sample	Element	XPS			TGA (Char % yield in N_2)	
		As-prepared	400 ℃	1000 ℃	at 800 ℃	at 1000 ℃
Graphite	C (%)	98.35	NA[a]	NA	99.7	99.1
	O (%)	1.65	NA	NA		
	C/O	59.6	NA	NA		
NGnP	C (%)	77.08	79.48	89.80	77.7	72.7
	O (%)	13.38	7.92	5.00		
	N (%)	8.47	12.6	5.2		
	C/O	7.7	13.4	23.9		
	C/N	10.6	7.4	20.1		
	5N/6N	2.9	2.0	1.4		

a. NA = Not applicable.

Table S4. Zeta-potentials of the pristine graphite and NGnPs at different concentrations

Sample	Concentration (mg/mL)			Particle Size (nm)
	0.10	0.05	0.02	
NGnP	-31.9	-35.3	-42.4	100

TableS5. EIS parameters on symmetrical dummy cells with the Pt-FTO and NGnP-FTO CEs , and exchange current density (J_0) calculated from R_{CT} values

CE	R_S (Ω cm^2)	R_{CT} (Ω cm^2)	CPE:1/B (S.s$^{\beta}$)	CPE:β	J_0 (mA/cm^2)
Pt	2.2	2.6	2.5×10^{-5}	0.93	9.88
NGnP	1.1	1.9	1.9×10^{-4}	0.77	10.3

TableS6. Photovoltaic performance of the DSSCs with Pt-FTO and NGnP-FTO CEs

CE	J_{SC}(mA/cm^2)	V_{OC}(mV)	FF(%)	PCE(%)
Pt	14.113	886	70.8	8.85
NGnP	14.162	890	74.1	9.34

Table S7. ElS analysis results of the DSSCs with Pt-FTO and NGnP-FTO CEs

CE	R_S (Ω cm^2)	R_{CT} (Ω cm^2)	R_{TR} (Ω cm^2)
Pt	2.27	4.62	18.04
NGnP	2.37	2.95	20.44

Table S8. Capacitance and capacity retention after 100 cycles of the pristine graphite, NGnPs and Pt/C at a scan rate of 0.01 V/s in N_2- and O_2-saturated 0.1 M aq. KOH solution

Sample	Capacitance (F/g)		Capacity Retention (%)	
	N_2	O_2	N_2	O_2
Graphite	3.9	43.5	98.5	92.1
NGnP	126.6	161.3	99.6	95.5
Pt/C	83.8	181.5	82.0	81.6

Table S9. Kinetic current (j_k) and average number of electrons (n_i) transferred for oxygen reduction at different potentials for the pristine graphite, NGnPs and Pt/C at a scan rate of 0.1 V/s in O_2-saturated 0.1 M aq. KOH solution

Sample	-0.4 V	-0.5 V	-0.6 V	-0.7 V
Graphite	2.2	2.1	2.2	2.2
NGnP	3.9	3.9	4.0	4.0
Pt/C	3.8	3.7	3.8	3.9

Table S10. Comparison of ORR electrocatalytic performance between NGnPs and N-graphene from literature report for metal-free ORR catalysts in alkaline electrolytes*

Sample	Method	Onset potential (V)[a]	Peak potential (V)[b]	Electron transferred number (n)	Reference
NGnP[c]	Ball-milling graphite in the presence of N_2	-0.14	-0.28	4.0	This work
N-graphene[d]	CVD of methane in the presence of NH_3	ca. -0.15[e]	ca. -0.40[e]	4.0	S22
N-CNT[f]	CVD of iron(II) phthalocyanine	ca. -0.15[e]	ca. -0.19[e]	3.9	S23

* All samples were measured in an Ag/AgCl as reference electrode in O_2 saturated 0.1M aq. KOH solution.

a.All samples were measured in O_2-saturated 0.1M aq. KOH solution by RDE or RRDE.

b. Measured by CV.

c. Scan rate at 0.01 V/s, electrode rotating speed at 1600 rpm and potential at -0.7 V.

d. Scan rate at 0.10 V/s, electrode rotating speed at 1000 rpm and potential at -0.8 V.

e. The value was estimated from the Figure in reported literatures.

g. Scan rate at 0.10 V/s, electrode rotating speed at 1400 rpm and potential at -0.3 V.

References

S1. Hohenberg, P. & Kohn, W. Inhomogeneous electron gas. *Phys. Rev.* **136**, B864-B871 (1964).

S2. Kresse, G. & Furthmüller, J. Efficient iterative schemes for ab initio total-energy calculations using a plane-wave basis set. *Phys. Rev. B* **54**, 11169-11186 (1996).

S3. Kresse, G. & Furthmüller, J. Efficiency of ab-initio total energy calculations for metals and semiconductors using a plane-wave basis set. *Comput. Mater. Sci.* **6**, 15-50 (1996).

S4. Kohn, V. & Sham, L. Self-consistent equations including exchange and correlation effects. *Phys. Rev.* **140**, A1133-A1138 (1965).

S5. Perdew, J. P., Burke, K. & Ernzerhof, M. Generalized gradient approximation made simple. *Phys. Rev. Lett.* **77**, 3865-3868 (1996).

S6. Lim, K., *et al.* Enhancing the performance of organic dye-sensitized solar cells via a slight structure modification. *J. Phys. Chem. C* **115**, 22640-22646 (2011).

S7. Tsao, H. N., *et al.* Cyclopentadithiophene bridged donor–acceptor dyes achieve high power conversion efficiencies in dye-sensitized solar cells based on the tris-cobalt bipyridine redox couple. *ChemSusChem* **4**, 591-594 (2011).

S8. Hauch, A. & Georg, A. Diffusion in the electrolyte and charge-transfer reaction at the platinum electrode in dye-sensitized solar cells. *Electrochim. Acta* **46**, 3457-3466 (2001).

S9. Murakami, T. N., *et al.* Highly efficient dye-sensitized solar cells based on carbon black counter electrodes. *J. Electrochem. Soc.* **153**, A2255-A2261 (2006).

S10. Liberatore, M., *et al.* Using EIS for diagnosis of dye-sensitized solar cells performance. *J. Appl. Electrochem.* **39**, 2291-2295 (2009).

S11. Wang, G., Xing, W. & Zhuo, S. Application of mesoporous carbon to counter

electrode for dye-sensitized solar cells. *J. Power Sources* **194**, 568-573 (2009).

S12. Trancik, J. E., Barton, S. C. & Hone, J. Transparent and catalytic carbon nanotube films. *Nano Lett.* **8**, 982-987 (2008).

S13. Kavan, L., Yum, J. H. & Grätzel, M. Optically transparent cathode for dye-sensitized solar cells based on graphene nanoplatelets. *ACS Nano* **5**, 165-172 (2011).

S14. Kavan, L., Yum, J. H. & Grätzel, M. Graphene nanoplatelets outperforming platinum as the electrocatalyst in Co-bipyridine-mediated dye-sensitized solar cells. *Nano Lett.* **11**, 5501-5506 (2011).

S15. Liberatore, M., *et al.* Mass transport and charge transfer rates for $Co^{(III)}/Co^{(II)}$ redox couple in a thin-layer cell. *Electrochim. Acta* **55**, 4025-4029 (2010).

S16. Han, L., Koide, N., Chiba, Y. & Mitate, T. Modeling of an equivalent circuit for dye-sensitized solar cells. *Appl. Phys. Lett.* **84**, 2433-2435 (2004).

S17. Sasaki, K., Zhang, L. & Adzic, R. R. Niobium oxide-supported platinum ultra-low amount electrocatalysts for oxygen reduction. *Phys. Chem. Chem. Phys.* **10**, 159-167 (2008).

S18. Chen, W. & Chen, W. Oxygen electroreduction catalyzed by gold nanoclusters: strong core size effects. *Angew. Chem. Int. Ed.* **48**, 4386-4389 (2009).

S19. Sarapuu, A., et al., Electrochemical reduction of oxygen on nanostructured gold electrodes. *J. Electroanal. Chem.* **612**, 78-86 (2008).

S20. Fabregat-Santiago, F., et al. Correlation between photovoltaic performance and impedance spectroscopy of dye-sensitized solar cells based on ionic liquids. *J. Phys. Chem. C* **111**, 6550-6560 (2007).

S21. Zhang, S., Shao, Y., Yin, G. & Lin, Y. Electrostatic self-assembly of a Pt-around-Au nanocomposite with high activity towards formic acid oxidation. *Angew. Chem. Int. Ed.* **49**, 2211-2214 (2010).

S22. Qu, L., Liu, Y., Baek, J. -B. & Dai, L. Nitrogen-doped graphene as efficient metal-free electrocatalyst for oxygen reduction in fuel cells. *ACS Nano* **4**, 1321-1326 (2010).

S23. Gong, K., Du, F., Xia, Z., Durstock, M. & Dai, L. Nitrogen-doped carbon nanotube arrays with high electrocatalytic activity for oxygen reduction. *Science* **323**, 760-764 (2009).